

# Experimental quantum reservoir computing with a circuit quantum electrodynamics system

B. Carles,<sup>1</sup> J. Dudas,<sup>1</sup> L. Balembois,<sup>2</sup> J. Grollier,<sup>1</sup> and D. Marković<sup>1</sup>

<sup>1</sup>*Laboratoire Albert Fert, CNRS, Thales, Université Paris-Saclay, 91767 Palaiseau, France*

<sup>2</sup>*SPEC, CEA, Gif-sur-Yvette, France*

(Dated: June 30, 2025)

Quantum reservoir computing is a machine learning framework that offers ease of training compared to other quantum neural network models, as it does not rely on gradient-based optimization. Learning is performed in a single step on the output features measured from the quantum system. Various implementations of quantum reservoir computing have been explored in simulations, with different measured features. Although simulations have shown that quantum reservoirs present advantages in performance compared to classical reservoirs, experimental implementations have remained scarce. This is due to the challenge of obtaining a large number of output features that are nonlinear transformations of the input data. In this work, we propose and experimentally implement a novel quantum reservoir computing platform based on a circuit quantum electrodynamics architecture, consisting of a single cavity mode coupled to a superconducting qubit. We obtain a large number of nonlinear features from a single physical system by encoding the input data in the amplitude of a coherent drive and measuring the cavity state in the Fock basis. We demonstrate classification of two classical tasks with significantly smaller hardware resources and fewer measured features compared to classical neural networks. Our experimental results are supported by numerical simulations that show additional Kerr nonlinearity is beneficial to reservoir performance. Our work demonstrates a hardware-efficient quantum neural network implementation that can be further scaled up and generalized to other quantum machine learning models.

Neural networks consist of layers of interconnected neurons that apply nonlinear transformations to input data. These layers are linked by synapses, whose weights are optimized during training. This architecture enables the network to extract features from input data that are *a priori* nonlinearly separable, ultimately allowing classification by a final linear layer. In software-based neural networks, training is typically performed through gradient descent. However, in hardware neural networks, computing the gradients of the output with respect to the synaptic weights is not straightforward: the transfer function is often unknown, and in quantum systems, efficient classical simulation is fundamentally impossible. This is where reservoir computing becomes a compelling alternative for hardware neural networks, including quantum implementations.

Reservoir computing uses the dynamics of a physical system to perform complex nonlinear transformations on input data, akin to the hidden layers of a deep neural network [1]. Quantum reservoir computing extends this concept to the quantum domain, embedding features in the high-dimensional quantum Hilbert space [2]. Quantum dynamics creates correlations between different input values, by constructing coherences between different degrees of freedom [3]. Feature extraction occurs via quantum measurements, with the resulting features classified by a subsequent linear layer. Nonlinearity in quantum reservoir computing can arise from the input data encoding [4], the quantum dynamics itself (e.g., through the Kerr effect [5, 6]), or the projective quantum measurement process [7–10]. Given that quantum machine learning holds the greatest promise for applications in-

volving quantum input data [11–14], where the quantum reservoir interfaces with a quantum system to classify its states, nonlinearity must not depend solely on the encoding process. Instead, we focus on exploring nonlinearity arising from the measurement process, which is critical for such quantum-native learning tasks.

In reservoir computing, the learning process occurs entirely on the extracted features, represented by the dashed lines in Figure 1(a). Thus, in order to ensure effective learning, a large number of features must be measured. Previous approaches addressed this by either increasing the number of measured qubits [15, 16], using multiplexing [9] or post-processing the measured data to calculate higher order statistical moments and provide more features [8]. In this work, we propose to extract the maximum information from a bosonic mode, by measuring it in the Fock basis and using occupation probabilities as neural activation functions. In this way, we obtain a large number of features that are nonlinear transformations of the input data.

We use a superconducting circuit composed of a Tantalum coplanar waveguide resonator capacitively coupled to a transmon qubit (Figure 1(b) and (c)). We use the fundamental  $\lambda/2$  mode of the resonator as a cavity, at a frequency  $\omega_c = 2\pi \times 7.617$  GHz. The system can be described by the Hamiltonian

$$\hat{H} = \hbar\omega_c \hat{a}^\dagger \hat{a} + \hbar\omega_q \frac{\sigma_Z}{2} - \hbar\frac{\chi}{2} \hat{a}^\dagger \hat{a} \sigma_Z, \quad (1)$$

where  $\omega_q = 2\pi \times 6.210$  GHz is the bare qubit frequency and  $\chi = 2\pi \times 22.29$  MHz is the dispersive shift that makes the cavity resonance frequency depend on the qubit state.

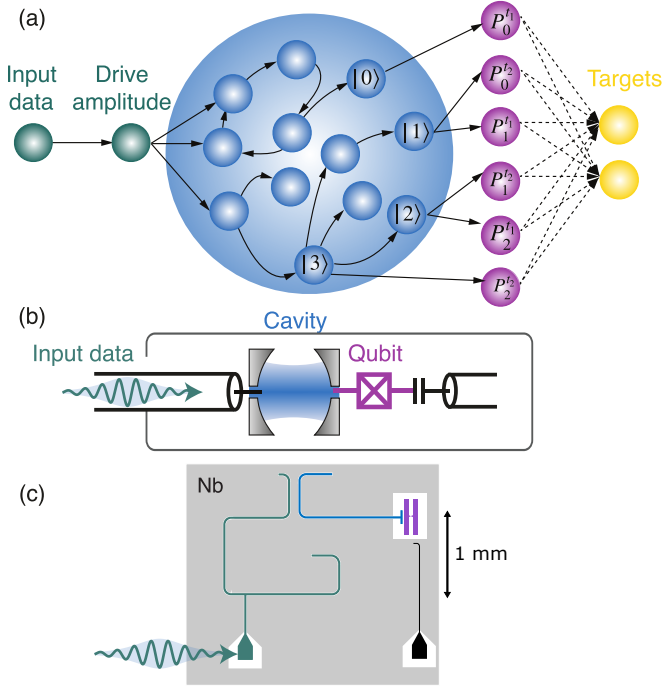


Figure 1: (a) Quantum reservoir computing. Input data is encoded in the amplitude of the resonant drive (green) of the quantum system (blue). Output features (purple circles) are obtained by measuring the occupation probabilities of Fock states  $|0\rangle$  to  $|n\rangle$  at different times  $t_1$  and  $t_2$ , yielding a total of  $2n$  output features. Features are classified by training a layer of linear weights (dashed lines). (b) Schematic and (c) design of the quantum circuit used to implement the quantum reservoir. Input data is mapped on the amplitude of a drive that is applied on the resonance of the fundamental mode of a Tantalum coplanar waveguide resonator. A transmon qubit is capacitively coupled to the cavity and to a transmission line.

Similarly, the qubit resonance frequency depends on the number of photons  $n = \langle \hat{a}^\dagger \hat{a} \rangle$  in the cavity. Indeed, in the two tone spectroscopy shown in Figure 2(a), we observe a set of equally spaced drive frequencies that lead to a significant shift of the cavity resonance. These drive frequencies, separated by  $\chi$ , correspond to resonance frequencies  $\omega_q^n = \omega_q - n\chi$  of the qubit dressed by  $n$  photons in the cavity. At higher input amplitudes  $\alpha_{\text{in}}$ , the probability to have a larger number of photons is larger, such that resonances at  $\omega_q^n$  for higher  $n$  are more pronounced.

We use this phenomenon to measure the number of photons in the cavity, and to infer the Fock state occupation probabilities from the measurement statistics. The time sequence used to measure the occupation probabilities is shown in the top of Figure 2(b). A 200 ns cavity displacement pulse  $D_\alpha$  is applied at cavity resonance, followed by a photon number-conditioned  $\pi_n$  pulse applied to the qubit at frequency  $\omega_q^n$ . The state of the qubit is

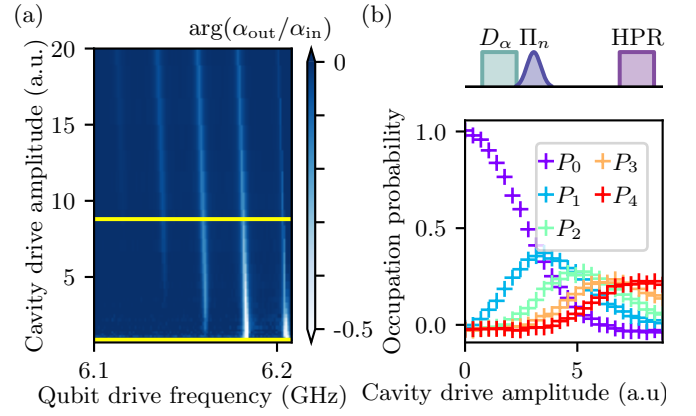


Figure 2: (a) Two tone spectroscopy of the cavity. The phase shift of the reflection coefficient at the cavity resonance frequency, as a function of the qubit drive frequency  $f_{\text{drive}}$  and the amplitude of the cavity readout tone. Different resonances from right to left correspond to the qubit frequency dressed by 0, 1, 2, 3 and 4 photons in the cavity. Yellow horizontal line corresponds to the maximum amplitude used for the data encoding. (b) Top: pulse sequence used to measure the photon number in the cavity. A 200 ns displacement pulse  $D_\alpha$  at cavity resonance frequency is followed by a 200 ns  $\pi_n$  pulse conditioned on  $n$  photons in the cavity, and a high power readout (HPR) after the 1  $\mu\text{s}$  waiting time. Bottom: Measured occupation probabilities  $P_0$  to  $P_4$  for Fock states  $|0\rangle$  to  $|4\rangle$  as a function of the amplitude  $\alpha_{\text{in}}$  of the cavity drive. Each point is averaged 10 000 times.

read through the same resonator, using high-power readout [17]. If the qubit is found in the excited state, we can increase the number of counts in the  $n$  photon bin by one, otherwise we discard the measurement. High power readout requires to precisely calibrate the readout amplitude, such that it leads the resonator to bifurcate only if the qubit is excited (see Supp. Mat.). For this reason, we perform the readout 1  $\mu\text{s}$  after the  $\pi_n$  pulse, letting enough time for the resonator to empty, such that the readout pulse is not affected by residual photons from the input data. In future experiments, this delay could be reduced by employing a dedicated readout resonator coupled to the qubit.

Measured occupation probabilities as a function of the input amplitude  $\alpha_{\text{in}}$  are shown in Figure 2(b). We observe that they are nonlinear functions, such that we can use them as neural activation functions, although they are all different, and not as monotonic as sigmoid, ReLu or tanh typically used in artificial neural networks. To perform learning on classical data, we map the classical input values on the cavity drive amplitude and we measure the occupation probabilities as neural outputs. The difficulty is that, inevitably, the cavity inherits some nonlinearity from the qubit, leading to a Kerr effect that can

be described by the Kerr Hamiltonian

$$\hat{H}^K = K_{cc}(\hat{a}^\dagger \hat{a})^2 - K_{cq}(\hat{a}^\dagger \hat{a})^2 \hat{\sigma}_Z, \quad (2)$$

where  $K_{cc}$  the cavity self-Kerr, and  $K_{cq}$  the cross-Kerr coefficient between the cavity and the qubit. Due to the self-Kerr effect, the cavity mode frequency shifts at high input amplitudes corresponding to large data values. Within the encoding range  $\alpha_{\text{in}} \in [0, 5]$ , this results in a cavity resonance shift of  $\Delta f_c = 1.7$  MHz. Since the cavity bandwidth is  $\kappa_c = 0.429$  MHz, which is significantly smaller than the shift, the drive becomes off-resonant for large input amplitudes and fails to efficiently couple to the cavity mode. We solve this issue by sending short input pulses of duration  $\Delta t_{\text{in}} = 200$  ns, ensuring they are broad enough to satisfy  $\Delta t_{\text{in}}^{-1} = 5$  MHz  $>$   $\Delta f_c$ .

The second constraint comes from the cross-Kerr effect between the qubit and the cavity, which shifts the qubit resonance frequency depending on the input power in the cavity. This shift reduces the efficiency of the conditional  $\pi_n$  pulse and, consequently, the overall readout efficiency.

We first implement sine and square waveform classification task, that consists in sending one by one points that belong either to a sine or to a square, and assigning them the correct label, as shown in Figure 3(a). This task tests the nonlinearity and memory of the underlying physical system, as it can be solved at best with 62.5% by a fully linear network, and at 87.5% by a nonlinear network without memory. We measure the occupation probabilities of states  $|0\rangle$  to  $|4\rangle$  after  $t_i = i \times 50$  ns,  $i \in [1, 4]$ . Each probability is reconstructed from 4000 measurements. This procedure yields 20 output features, corresponding to 5 probabilities at 4 different times.

The prediction  $Y = FW$  is obtained by multiplying the feature matrix  $F$  by the weight matrix  $W$ . We use half of the dataset for training, during which  $W$  is computed by multiplying the target vector  $\tilde{Y}$  with the pseudoinverse of the feature matrix  $W = F^{-1}\tilde{Y}$ . The prediction on the test set—the second half of the data points not used in training—matches the target with 99.7 % accuracy. Remarkably, even when retaining only the eight most informative neurons, we still achieve 99.5 % accuracy, as shown in Figure 3(c). This result is consistent with previous simulations [7], which demonstrated that this task can be solved using only 9 quantum features, whereas at least 25 classical features are required to achieve comparable performance, and confirms the role of quantum coherence in learning [18].

Second, we implement the Mackey-Glass chaotic time series prediction task [19], which consists in forecasting future values of a time series based on its past values. The time series is generated as a solution of the Mackey-Glass nonlinear differential equation (see Supplementary Material) and is shown in Figure 4(a). Performance is evaluated using the normalized root mean square error (NRMSE) between the predicted and target values. The

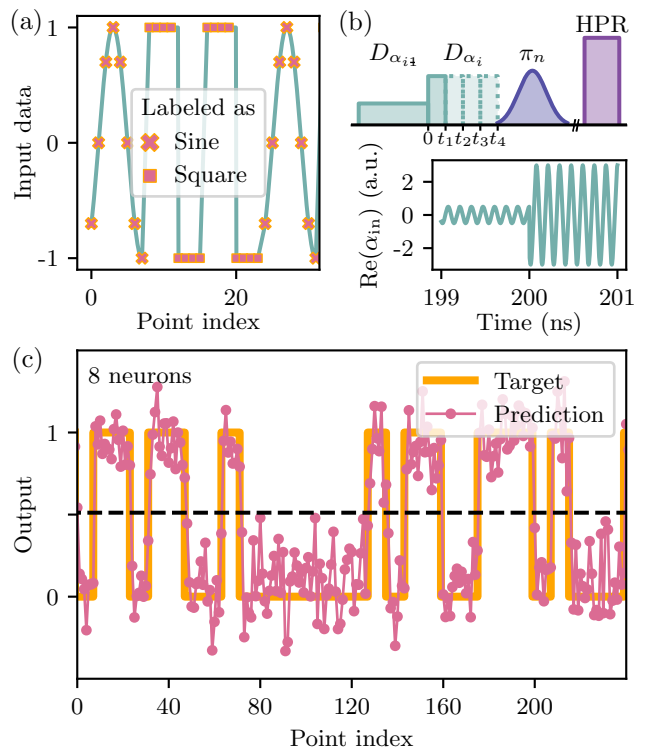


Figure 3: (a) Input data for the sine and square waveform classification task. A random series of 400 sine and square periods is discretized in 8 points per period. Only 4 periods are shown for clarity. (b) Top: pulse sequence consists of two displacement pulses with amplitudes corresponding to two consequent data points, followed by a  $\pi_n$  pulse and high-power readout. To increase the number of extracted features, the occupation probabilities are measured after four different durations  $t_1$  to  $t_4$  of the second displacement pulse. Bottom: Cavity drive  $\text{Re}(\alpha_{\text{in}})$  whose amplitude encodes the input data. (c) Prediction of the quantum reservoir with the 8 most informative features among probabilities of states  $|0\rangle$  to  $|4\rangle$  at times  $t_i = i \times 50$  ns,  $i \in [1, 4]$ .

error increases with delay  $d$  up to  $d = 14$ , then decreases—reflecting the periodicity in the input data—and increases again beyond  $d = 26$ , which corresponds to  $2.6 \mu\text{s}$ , i.e., more than twice the cavity lifetime  $2T_c$ .

Having experimentally demonstrated the classification of sine and square waveforms, as well as the prediction of a chaotic time series using a quantum reservoir, we now turn to simulations to explore the physical origin of the reservoir’s computational capabilities. In particular, we investigate how the Kerr nonlinearity—which plays a central role in shaping the system’s dynamics—affects performance.

The effect of different types and magnitudes of nonlinearities on the performance of quantum neural networks remains an open question [20, 21]. In optical quantum

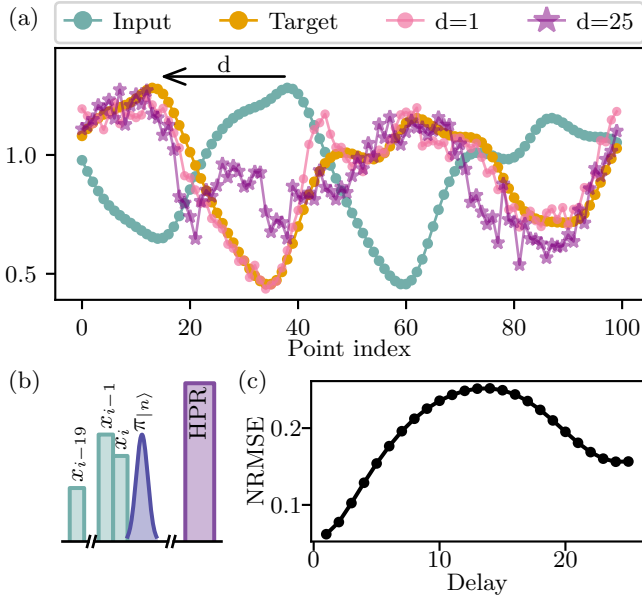


Figure 4: (a) Mackey-Glass chaotic time series (green). The task is to predict the value at time  $t+d$  based on the 20 preceding data points. The target (gold) corresponds to the time series shifted by  $d$  steps. Quantum reservoir predictions for delays  $d = 1$  and  $d = 25$  are shown in pink and purple, respectively. (b) Pulse sequence: 20 displacement pulses of 100 ns each, followed by the read-out of populations in states  $|0\rangle$  to  $|4\rangle$ . (c) Normalized root mean square error (NRMSE) as a function of delay  $d$ .

neural networks, some studies have suggested that weaker Kerr nonlinearities lead to degraded performance [22]. In the context of bosonic quantum neural networks, it has been shown that while simple classical tasks such as XOR gate learning can be solved with only encoding nonlinearity, quantum tasks require an additional Kerr nonlinearity, which also improves robustness to errors and noise [23].

To investigate the influence of Kerr nonlinearity in our setup, we simulate the classification of sine and square waveforms using a Kerr oscillator with varying Kerr coefficients  $K_{cc}$ . In the frame rotating at the resonator frequency  $\omega_c$ , the Hamiltonian is

$$\hat{H} = \hbar\Delta\hat{a}^\dagger\hat{a} + K_{cc}(\hat{a}^\dagger\hat{a})^2 \quad (3)$$

where  $\Delta$  is the input drive detuning from the cavity resonance. We solve the Lindblad master equation, with  $\kappa_{\text{in}} = 2\pi \times 597.4$  kHz and  $\kappa_{\text{loss}} = 2\pi \times 472.9$  kHz as in the experiment. Since the input drive is applied at a fixed frequency for all drive amplitudes, its coupling to the resonator becomes less efficient when the Kerr coefficient is large. This significantly affects the number of photons inside the mode. As shown in Figure 5(a), for large Kerr coefficients  $K_{cc}$  and zero detuning, the mean photon num-

ber in the cavity remains below 1. In this case, the drive is too far from the effective resonance to efficiently populate the cavity. At larger detunings, the mean photon number becomes a non-monotonic function of the drive amplitude  $\alpha_{\text{in}}$ : it initially increases, reaching a maximum at an intermediate amplitude where the drive frequency is closest to resonance, and then decreases again at higher amplitudes as the system moves away from resonance. This is why for large Kerr coefficients, it is potentially interesting to apply the input data at a frequency detuned by  $\Delta$  from the resonance.

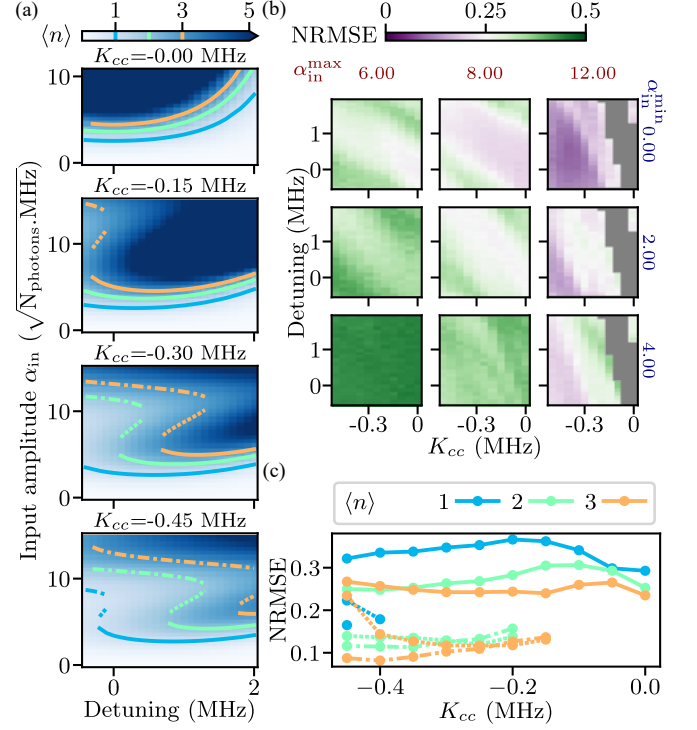


Figure 5: (a) Simulated mean photon number  $\langle n \rangle$  in the cavity after a 400 ns drive as a function of the drive amplitude  $\alpha_{\text{in}}$  and detuning, for different Kerr rates  $K_{cc}$ . Contour lines indicate regions of equal mean photon number. (b) Normalized root mean square error (NRMSE) for sine-square classification using 20 neurons, shown as a function of Kerr coefficient and detuning, for various input encoding ranges  $[\alpha_{\text{in}}^{\text{min}}, \alpha_{\text{in}}^{\text{max}}]$ . Gray pixels indicate parameter regions where the photon number exceeded the simulation space limits, rendering the classification results unreliable. (c) Simulated NRMSE as a function of Kerr coefficient for the encoding range  $[0.4 \alpha_0, 1.6 \alpha_0]$ , where  $\alpha_0$  is the drive amplitude required to reach  $\langle n \rangle \in \{1, 2, 3\}$  after a 400 ns drive (see panel (a)). Because multiple combinations of detuning and amplitude can yield the same mean photon number, the optimal NRMSE values for different amplitudes are shown with distinct line styles.

We study the performance on the sin-square task as a

function of Kerr coefficient  $K_{cc}$ . In order to separate the impact of the additional nonlinearity from the spurious effects such as the photon number in the cavity related to the frequency shift, we perform the study for different drive detunings and also for different encoding ranges  $[\alpha_{\min}, \alpha_{\max}]$  as shown in Figure 5(b). We evaluate the performance using the normalized root mean square error

$$\text{NRMSE} = \frac{1}{\tilde{y}_{\max} - \tilde{y}_{\min}} \sqrt{\frac{\sum_i^N (y_i - \tilde{y}_i)^2}{N}}. \quad (4)$$

We observe that the lowest classification errors are achieved for the largest encoding ranges and for high values of the Kerr coefficient.

To isolate the contribution of the Kerr effect from that of the amplitude encoding range, we proceed as follows: for a given Kerr coefficient and a fixed target mean photon number  $\langle n \rangle \in \{1, 2, 3\}$ , we select all combinations of  $\{\Delta, \alpha_0\}$  such that the lowest input amplitude results in  $\langle n \rangle$  photons in the cavity. We then define the encoding range as  $[0.4\alpha_0, 1.6\alpha_0]$ . The corresponding normalized root-mean-square error (NRMSE) is shown in Figure 5(c). We observe that the lowest errors are obtained for large Kerr coefficients. It is important to note that for a given Kerr coefficient, the same mean photon number can be achieved with different drive amplitudes, due to the non-monotonic behavior of the photon number as a function of input amplitude, as shown in Figure 5(a). This explains the presence of multiple points with the same Kerr coefficient but different amplitudes in Figure 5(c). Lower errors are generally associated with higher drive amplitudes.

In conclusion, we have demonstrated quantum reservoir computing using a bosonic mode coupled to a qubit. Input data are encoded into the amplitudes of coherent drives, while the system's response is read out in the Fock basis, enabling efficient information extraction without requiring complex post-processing. Nonlinearity arises both from the measurement process and from the Kerr effect induced by the qubit used for readout. Since the Kerr nonlinearity shifts the cavity resonance, we developed an approach based on short input pulses, which broadens the effective frequency bandwidth and ensures robust encoding.

To investigate the role of Kerr nonlinearity—an open question in quantum reservoir computing—we performed simulations isolating its influence on classification performance. The results show that the Kerr effect enhances performance, especially in regimes where input amplitudes interact non-trivially with detuned resonator dynamics. These findings suggest that Kerr-induced nonlinearity is a valuable resource. Future work will explore its role in broader computational settings, including temporal and quantum tasks, to fully harness the potential

of Kerr-enhanced quantum reservoirs.

## ACKNOWLEDGMENTS

The authors thank E. Flurin (SPEC, CEA, Gif-sur-Yvette, France) for his help in the sample fabrication and advice on performing the circuit measurements. This research was supported by the Paris Ile-de-France Region in the framework of DIM SIRTEQ and by European Union (ERC, qDynnet, 101076898).

- 
- [1] H. Jaeger, *The "echo state" approach to analysing and training recurrent neural networks*, GMD Report 148 (GMD - German National Research Institute for Computer Science, 2001).
  - [2] K. Fujii and K. Nakajima, *Physical Review Applied* **8**, 024030 (2017).
  - [3] N. Götting, F. Lohof, and C. Gies, *Physical Review A* **108**, 052427 (2023), arXiv:2302.03595 [quant-ph].
  - [4] J. Nokkala, R. Martínez-Peña, G. L. Giorgi, V. Parigi, M. C. Soriano, and R. Zambrini, *Communications Physics* **4**, 53 (2021).
  - [5] L. C. G. Govia, G. J. Ribeill, G. E. Rowlands, H. K. Krovi, and T. A. Ohki, *Physical Review Research* **3**, 013077 (2021).
  - [6] G. Angelatos, S. A. Khan, and H. E. Türeci, *Physical Review X* **11**, 041062 (2021).
  - [7] J. Dudas, B. Carles, E. Plouet, F. A. Mizrahi, J. Grollier, and D. Marković, *npj Quantum Information* **9**, 64 (2023).
  - [8] A. Senanian, S. Prabhu, V. Kremenetski, S. Roy, Y. Cao, J. Kline, T. Onodera, L. G. Wright, X. Wu, V. Fatemi, and P. L. McMahon, *Nature Communications* **15**, 7490 (2024).
  - [9] F. Hu, S. A. Khan, N. T. Bronn, G. Angelatos, G. E. Rowlands, G. J. Ribeill, and H. E. Türeci, *Nature Communications* **15**, 7491 (2024).
  - [10] K. Kobayashi, K. Fujii, and N. Yamamoto, *PRX Quantum* **5**, 040325 (2024).
  - [11] S. Ghosh, A. Opala, M. Matuszewski, T. Paterek, and T. C. H. Liew, *npj Quantum Information* **5**, 35 (2019).
  - [12] D. Marković and J. Grollier, *Applied Physics Letters* **117**, 150501 (2020).
  - [13] H.-Y. Huang, M. Broughton, J. Cotler, S. Chen, J. Li, M. Mohseni, H. Neven, R. Babbush, R. Kueng, J. Preskill, and J. R. McClean, *Science* **376**, 1182 (2022).
  - [14] Q. H. Tran and K. Nakajima, *Physical Review Letters* **127**, 260401 (2021).
  - [15] M. Kornjača, H.-Y. Hu, C. Zhao, J. Wurtz, P. Weinberg, M. Hamdan, A. Zhdanov, S. H. Cantu, H. Zhou, R. A. Bravo, K. Bagnall, J. I. Basham, J. Campo, A. Choukri, R. DeAngelo, P. Frederick, D. Haines, J. Hammett, N. Hsu, M.-G. Hu, F. Huber, P. N. Jepsen, N. Jia, T. Karolyshyn, M. Kwon, J. Long, J. Lopatin, A. Lukin, T. Macrì, O. Marković, L. A. Martínez-Martínez, X. Meng, E. Ostroumov, D. Paquette, J. Robinson, P. S. Rodriguez, A. Singh, N. Sinha, H. Thoreen, N. Wan, D. Waxman-Lenz, T. Wong, K.-H. Wu, P. L. S. Lopes, Y. Boger, N. Gemelke, T. Kitagawa, A. Keesling, X. Gao, A. Bylinskii, S. F. Yelin, F. Liu, and S.-T. Wang, *Large-scale quantum reservoir learning with*

- an analog quantum computer (2024), arXiv:2407.02553 [cond-mat, physics:physics, physics:quant-ph].
- [16] C. Zhu, P. J. Ehlers, H. I. Nurdin, and D. Soh, Practical Few-Atom Quantum Reservoir Computing (2025), arXiv:2405.04799 [quant-ph].
  - [17] M. D. Reed, L. DiCarlo, B. R. Johnson, L. Sun, D. I. Schuster, L. Frunzio, and R. J. Schoelkopf, Physical Review Letters **105**, 10.1103/physrevlett.105.173601 (2010).
  - [18] A. Palacios, R. Martínez-Peña, M. C. Soriano, G. L. Giorgi, and R. Zambrini, Communications Physics **7**, 369 (2024).
  - [19] M. C. Mackey and L. Glass, Science **197**, 287 (1977).
  - [20] D. Stanev, N. Spagnolo, and F. Sciarrino, Physical Review Research **5**, 013139 (2023).
  - [21] A. Motamedi, H. Zadeh-Haghighi, and C. Simon, Quantumness and Learning Performance in Reservoir Computing with a Single Oscillator (2024), arXiv:2304.03462 [quant-ph].
  - [22] G. R. Steinbrecher, J. P. Olson, D. Englund, and J. Carolan, npj Quantum Information **5**, 60 (2019).
  - [23] H. Xu, T. Krisnanda, R. Bao, and T. C. H. Liew, New Journal of Physics **25**, 023028 (2023).